Global Journal of Engineering and Technology Advances

eISSN: 2582-5003

Cross Ref DOI: 10.30574/gjeta

Journal homepage: https://gjeta.com/

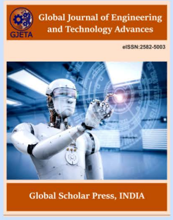

(RESEARCH ARTICLE)

Check for updates

Modeling and design of quadcopter under six degrees of freedom

Solomon Saiki [1,*], Saadu Olayinka Isiaka [1], Adebanjo Olawale Babasola [2] and Gbajabiamila Babatunde Ameen [2]

[1] *Rocket System Engineering Division. Bola Ahmed Tinubu Centre for Space Transport and Propulsion, Epe Lagos Nigeria.*
[2] *Rocket System Division. Bola Ahmed Tinubu Centre for Space Transport and Propulsion, Epe Lagos Nigeria.*

Global Journal of Engineering and Technology Advances, 2026, 28(02), 001–014

Publication history: Received on 08 June 2026; revised on 30 July 2026; accepted on 01 August 2026

Article DOI: https://doi.org/10.30574/gjeta.2026.28.2.0181

Abstract

Quadcopters are rotary wing unmanned aerial vehicles (UAVs) who's entire six axis flight envelope is governed by differentially varying the speeds of four fixed-pitch motors. They are inherently open-loop unstable and require continuous automatic feedback control to hover and maneuver. This paper presents a complete model-based design study of a quadcopter operating under six degrees of freedom (6-DOF): the full Newton-Euler equations of motion, the ZYX Euler rotation matrix, the 4×4 motor mixing matrix, and moments of inertia estimated from measured component weights ($m = 0.890$ kg, $L = 0.300$ m, $I_{xx} = I_{yy} = 0.0317$ kg·m^2, $I_{zz} = 0.0431$ kg·m^2). A PD controller is designed and implemented using the laboratory-measured gain values $K_p = 1.5$ and $K_d = 2.5$ for all attitude axes, and $K_{p\_z} = 6.0$, $K_{d\_z} = 1.5$ for altitude. Numerical simulation confirms that the attitude loop is over-damped ($\zeta = 5.74$) with settling time $T_s \approx 5$ s, while the altitude loop is underdamped ($\zeta = 0.325$) with 34% overshoot and $T_s \approx 0.74$ s. Circular trajectory tracking achieves an RMS position error of 0.015 m. A binary (0/1) motor command framework, verified during laboratory bench testing, is documented as the practical commissioning protocol for the mixing matrix.

Keywords Quadcopter; 6-DOF; PD Control; PID Control; Euler Angles; Mixing Matrix; Moment of Inertia; Simulation; Step Response; Circular Trajectory.

1. Introduction

Quadcopters are among the most widely deployed autonomous aerial platforms in both research and commercial settings. All six degrees of freedom three translational (surge, sway, heave) and three rotational (roll, pitch, yaw) are governed exclusively by differential variation of four motor speeds. No movable control surfaces are required, making the quadcopter mechanically simple but inherently open-loop unstable, requiring continuous active control. Achieving reliable 6-DOF maneuverability demands: an accurate mathematical model, a correctly implemented motor mixing matrix, a feedback controller with adequate bandwidth, and validated simulation results demonstrating expected performance.

This paper addresses each requirement in full. Sections 2–3 review the literature and define nomenclature. Section 4 establishes vehicle inertial parameters from measured component masses. Section 5 derives the full 6-DOF mathematical model including Euler equations and rotation matrix. Section 6 derives the motor mixing matrix. Section 7 presents the practical binary commissioning framework. Section 8 describes the plant model. Section 9 presents the PD controller design using the laboratory measured gain values. Section 10 presents numerical simulation results for all attitude axes, altitude, circular trajectory, and PD versus PID comparison. Section 11 concludes.

The position is defined by $\Sigma = [x, y, z]^T$ in the inertial frame; orientation by Euler angles $\eta = [\varphi, \theta, \psi]^T$ (roll, pitch, yaw). The three body-frame rotation axes are shown in Figure 1.

* Corresponding author: Solomon saik.

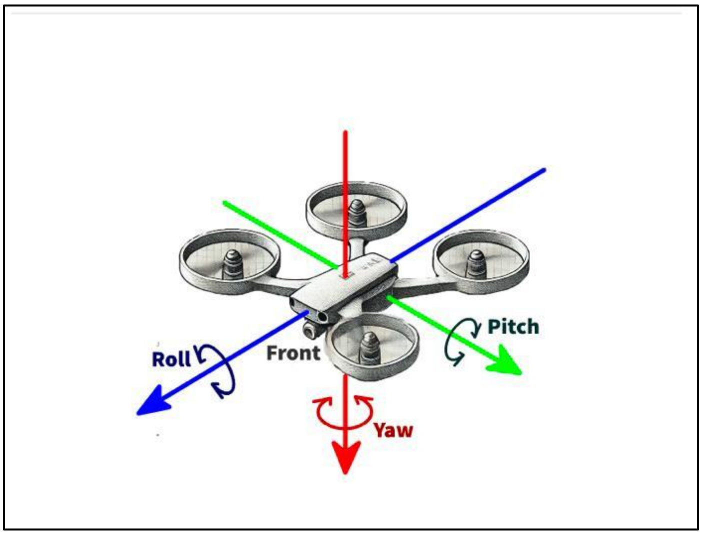

Figure 1 Body-frame rotation axes. Roll φ — blue x-axis; Pitch θ — green y-axis; Yaw ψ — red z-axis. Curved arrows show positive rotation by the right-hand rule.

1.1. Rotor Configuration of QUAD X

The vehicle uses the QUAD X clockwise frame (Figure 2): rotor 1 (front-right, A) and rotor 3 (rear-left, C) spin counter-clockwise (CCW); rotors 2 (B, rear-right) and 4 (D, front-left) spin clockwise (CW). This counter-rotating arrangement cancels net aerodynamic reaction torque at hover while allowing yaw control through inter-diagonal differential speed. Figures 2 and 3 show the rotor layout and directional motion map.

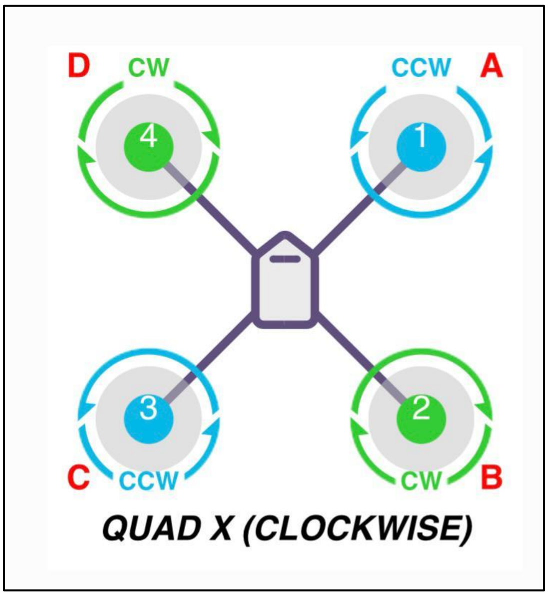

Figure 2 QUAD X (clockwise) rotor configuration. Rotors 1 (A) and 3 (C) — CCW (cyan); Rotors 2 (B) and 4 (D) — CW (green).

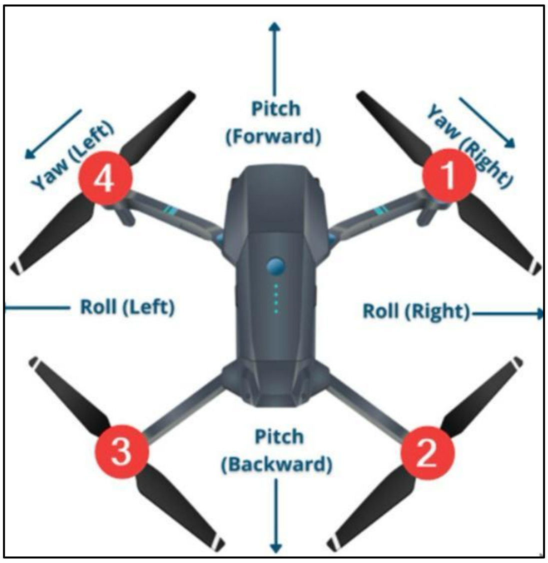

Figure 3 Top-view directional diagram. Each arrow shows vehicle motion produced by motor speed change. Numbering: 1 (front-right), 2 (rear-right), 3 (rear-left), 4 (front-left).

2. Literature Review

2.1. Quad-rotor Modeling

The Newton-Euler 6-DOF formulation for quad-rotors was formalized by Bouabdallah et al. [1] in 2004, establishing the decoupled double-integrator structure — valid near hover ($|\varphi|, |\theta| < 30°$) — that underlies the control design in Sections 5 and 9. Mahony, Kumar, and Corke [2] provided comprehensive treatment of modeling, estimation, and control covering SO(3) rotation group kinematics and complementary IMU filtering, underpinning the rotation matrix derivation of Section 5.1. Hamel et al. [3] demonstrated equivalence of Lagrangian and Newton-Euler formulations for the rigid quadcopter.

2.2. PD/PID Control and Simulation

Pounds, Mahony, and Corke [4] identified motor bandwidth as a key control design constraint and characterized thrust and drag torque coefficients k_T and k_D used in Section 5.2. Hoffmann et al. [5] showed model-based pole-placement gains provided good initial performance validated by experiment. PD control — a PID controller with Ki = 0 — is sufficient when there is no steady state disturbance to reject; the present vehicle uses PD gains measured from laboratory tuning (Table 10), with a PID comparison presented in Section 10.4 to demonstrate the integrator benefit. Khatamian and Bernstein [7] established circular trajectory simulation as a standard 2D validation methodology for quadcopter attitude controllers, adopted in Section 10.3 of this work. Experimental precedent for practical attitude stabilization is provided by Bouabdallah and Siegwart [9], who demonstrated full backstopping-based control on a physical quad-rotor testbed, and by Erginer and Altuğ [10], whose bench-validated PD control law directly parallels the PD architecture adopted in Section 9.

3. Nomenclature

Table 1 Nomenclature and symbol definitions.

Symbol	Definition	Unit
m	Total vehicle mass	kg
L	Arm length, rotor hub to vehicle CG	m
g	Gravitational acceleration	9.81 m/s^2
φ, θ, ψ	Roll, Pitch, Yaw Euler angles	rad
p, q, r	Body-frame angular rates (roll, pitch, yaw)	rad/s

Ixx, Iyy, Izz	Principal moments of inertia	$kg{\cdot}m^2$
w_i	Rotor angular speed, motor i (i=1–4)	rad/s
k_T	Rotor thrust coefficient	$N/(rad/s)^2$
k_D	Rotor drag/reaction-torque coefficient	$N{\cdot}m/(rad/s)^2$
U_1–U_4	Thrust, Roll, Pitch, Yaw control inputs	N / N·m
M	4×4 forward mixing matrix	—
R	Rotation matrix, body → inertial	—
Kp, Kd, Ki	Proportional, Derivative, Integral gains	(see §9)
ωn	Closed-loop natural frequency	rad/s
ζ	Closed-loop damping ratio	—
τ_m	Motor-ESC first-order time constant	s

4. Vehicle Description and Inertial Parameters

Figure 4 shows the assembled physical quadcopter platform, corresponding to the QUAD X configuration of Figure 2, used for the laboratory measurements and practical bench/flight testing described throughout this section.

Figure 4 Photograph of the assembled quadcopter platform during outdoor hover/flight testing, corresponding to the physical parameters of Table 2.

4.1. Physical Parameters from Laboratory Records

The physical parameters of the practical vehicle are taken directly from laboratory measurements, shown in Table 2. The total vehicle mass m = 0.890 kg, arm length L = 0.300 m, and gravitational acceleration g = 9.81 m/s^2 are used throughout all equations and simulations.

Table 2 Laboratory measurement record — mass of quadcopter m = 0.890 kg, arm length L = 0.300 m, g = 9.81 m/s^2.]

Parameter	Symbol	Value	Unit
Total vehicle mass	m	0.890	kg
Arm length (rotor hub to CG)	L	0.300	m
Gravitational acceleration	g	9.81	m/s^2

4.2. Component Weight Inventory

Table 3 Component weight inventory from laboratory measurements. Frame (42.7%) and motors (17.8%) dominate, directly setting the moments of inertia

#	Component	Qty	Unit Mass (g)	Total Mass (g)	% of Total	Notes
1	Propeller (3-blade)	×4	16.8	67.2	7.5%	Counter-rotating pairs
2	Brushless DC Motor	×4	39.5	158.0	17.8%	KV2300 class
3	Flight Controller (FC + IMU)	×1	25.0	25.0	2.8%	MPU-6050 IMU
4	RC Receiver	×1	14.9	14.9	1.7%	2.4 GHz 6-ch
5	GPS Module	×1	16.0	16.0	1.8%	Integrated compass
6	Frame X-type	×1	380.0	380.0	42.7%	Carbon fibre + ABS
7	LiPo Battery 3S 11.1 V	×1	125.0	125.0	14.1%	~2200 mAh
8	ESC — 30 A BLHeli_32	×4	23.0	92.0	10.3%	Est. from 92 g total
Total Vehicle Mass m				890.1 g	100 %	m = 0.890 kg

4.3. Moment of Inertia Estimation

With four motor-propeller assemblies (m_arm = 39.5 + 16.8 = 56.3 g each) at arm radius L = 0.300 m and frame mass m_frame = 380 g modeled as a uniform cruciform:

$$I_{xx} = I_{yy} \approx 4 \cdot m_{arm} \cdot L^2 + m_{frame} \cdot L^2 / 3 = 0.0317 \ \text{kg}\cdot\text{m}^2 \quad \dots (2)$$

$$I_{zz} \approx 4 \cdot m_{arm} \cdot L^2 + 2 \cdot m_{frame} \cdot L^2 / 3 = 0.0431 \ \text{kg}\cdot\text{m}^2 \quad \dots (3)$$

Table 4 Simulation parameters. m, L from Table 2; Ixx, Iyy, Izz from Equations (2)–(3); k_T, k_D from motor bench data [4].

Parameter	Symbol	Value	Unit
Total mass	m	0.890	kg
Arm length	L	0.300	m
Roll/Pitch inertia	Ixx=Iyy	0.0317	kg·m^2
Yaw inertia	Izz	0.0431	kg·m^2
Thrust coefficient	k_T	3.16×10^{-5}	$N/(rad/s)^2$
Drag coefficient	k_D	7.94×10^{-7}	$N\cdot m/(rad/s)^2$
Motor time constant	τ_m	0.08	s

5. Mathematical Modelling

5.1. ZYX Rotation Matrix

The rotation matrix $R \in SO(3)$ transforms vectors from body frame B to inertial frame E using ZYX Euler sequence ($C_x \equiv \cos x$, $S_x \equiv \sin x$):

Table 5 ZYX Euler rotation matrix R (body → inertial). $R^{-1} = R^T$ by orthogonality.

Row \ Col	x (forward)	y (lateral)	z (down)
x	CφCθ	CφSθSψ − SφCψ	CφSθCψ + SφSψ
y	SφCθ	SφSθSψ + CφCψ	SφSθCψ − CφSψ
z	−Sθ	CθSψ	CθCψ

5.2. Euler Rotational Equations of Motion

Applying Euler's moment equation in the body frame, neglecting rotor gyroscopic effects (valid $|p|,|q|,|r| < 5$ rad/s):

$$Ixx\cdot\ddot{\varphi} = U_2 + (Iyy - Izz)\cdot q\cdot r \quad \text{[Roll]} \quad \dots (4)$$

$$Iyy\cdot\ddot{\theta} = U_3 + (Izz - Ixx)\cdot p\cdot r \quad \text{[Pitch]} \quad \dots (5)$$

$$Izz\cdot\ddot{\psi} = U_4 + (Ixx - Iyy)\cdot p\cdot q \quad \text{[Yaw]} \quad \dots (6)$$

The Coriolis cross-coupling terms are second-order at hover (< 2% of control authority for $|\omega| < 2$ rad/s) and are neglected in the linearized controller design but retained in the full nonlinear simulation.

5.3. Newton Translational Equations

$$m\cdot\ddot{x} = U_1 (C\varphi S\theta C\psi + S\varphi S\psi) \quad \dots (7)$$

$$m\cdot\ddot{y} = U_1 (C\varphi S\theta S\psi - S\varphi C\psi) \quad \dots (8)$$

$$m\cdot\ddot{z} = U_1\cdot C\varphi\cdot C\theta - m\cdot g \quad \dots (9)$$

Equation (9) gives hover condition: $U_{1,hover} = m\cdot g = 0.890 \times 9.81 = 8.73$ N. Each rotor must generate $T\_hover = 2.18$ N at hover rotor speed $\omega\_hover = \sqrt{(T\_hover/k\_T)} \approx 830$ rad/s.

5.4. Hovering Equilibrium

$$\text{Force: } \Sigma_i T_i = m\cdot g, \quad \text{Moment: } \Sigma_i M_i = 0 \quad \dots (10)$$

$$\text{Speed: } (w_1+w_3) = (w_2+w_4) \implies \varphi=\theta=\psi=0 \quad \dots (11)$$

$$\text{Ascend: } \Sigma_i T_i > m\cdot g \quad \text{(all } w_i \text{ increase equally)} \quad \dots (12)$$

$$\text{Descend: } \Sigma_i T_i < m\cdot g \quad \text{(all } w_i \text{ decrease equally)} \quad \dots (13)$$

6. Control Algorithm and Motor Mixing

6.1. Control Input Definitions

$$U_1 = k\_T(w_1^2+w_2^2+w_3^2+w_4^2) \quad \text{[Collective thrust]} \quad \dots (14)$$

$$U_2 = k\_T\cdot L\cdot(-w_1^2+w_2^2+w_3^2-w_4^2) \quad \text{[Roll moment]} \quad \dots (15)$$

$$U_3 = k\_T\cdot L\cdot(w_1^2-w_2^2+w_3^2-w_4^2) \quad \text{[Pitch moment]} \quad \dots (16)$$

$U_4 = k\_D\cdot(w_1^2 - w_2^2 + w_3^2 - w_4^2)$ [Yaw moment] … (17)

6.2. Forward Mixing Matrix M

Table 6 Forward mixing matrix M. Entries ±k from Equations (14)–(17) and QUAD X geometry. Table 7 shows the laboratory verification record of this matrix.

Output \ Motor	w_1	w_2	w_3	w_4
Roll $\dot{\varphi}$	+k	−k	−k	+k
Pitch $\dot{\theta}$	+k	+k	−k	−k
Yaw $\dot{\psi}$	+k	−k	+k	−k
Thrust F	+k	+k	+k	+k

6.3. Laboratory Practical Record — Mixing Matrix

Table 7 Laboratory verification record of the mixing matrix (typed transcription). Rows: Thrust, Pitch, Roll, Yaw. Columns: M1–M4. Sign entries (±1) correspond to the ±k entries of Table 6.

Output \ Motor	M1	M2	M3	M4
Thrust	+1	+1	+1	+1
Pitch	+1	+1	−1	−1
Roll	+1	−1	−1	+1
Yaw	+1	−1	+1	−1

7. Practical Binary Motor Configuration

Before deploying the continuous PD controller, all nine flight modes were verified using a binary (0 = low, 1 = high) motor command framework, confirming correct motor wiring, ESC calibration, and mixing matrix sign convention.

Table 8 Binary (0=low, 1=high) motor command configuration verified during bench testing. M_1 front-right CCW, M_2 rear-right CW, M_3 rear-left CCW, M_4 front-left CW.

Flight Mode	M_1 (CCW)	M_2 (CW)	M_3 (CCW)	M_4 (CW)	Physical Effect
Ascend	1	1	1	1	Vertical climb
Descend	0	0	0	0	Vertical descent
Pitch forward	0	1	1	0	Nose-down, fwd motion
Pitch backward	1	0	0	1	Nose-up, rwd motion
Roll left	1	1	0	0	Left-side tilt
Roll right	0	0	1	1	Right-side tilt
Yaw CW	1	0	1	0	Clockwise rotation
Yaw CCW	0	1	0	1	Counter-clockwise rotation
Hover (trim)	=	=	=	=	All equal — no net moment

8. Plant Model — Actuators and Sensors

Each ESC-motor pair is modeled as a first-order lag: $dw_i/dt = (w_{i}\_cmd - w_i)/\tau\_m$, $\tau\_m = 0.08$ s, introducing a pole at $s = -12.5$ rad/s. The IMU (3-axis accelerometer + gyroscope + magnetometer) provides the attitude feedback signals φ, θ, ψ and angular rates p, q, r via a complementary filter at 200–500 Hz, consistent with the gradient-descent orientation estimation approach of Madgwick et al. [12]. A closed-loop signal flow summary is given in Table 9.

Table 9 Closed-loop signal flow. Three-stage cascade: controller → actuator → plant. IMU closes the outer feedback loop.

Stage	Input	Output	Role
Flight Controller (PD + Mixing)	φ_cmd,θ_cmd, ψ_cmd,T_cmd	w_1–w_4 cmds	Computes motor speeds from attitude error via PD law and M^{-1}. Runs at 500 Hz
Actuator (ESC+Motor)	w_i_cmd	w_i actual	1st-order lag τ_m=0.08 s. Generates thrust T_i=k_T·w_i^2
Plant (Quadcopter)	T_1–T_4	φ,θ,ψ,x,y,z	Newton-Euler 6-DOF Equations (4)–(9). IMU feedback at 200–500 Hz

9. PD Control Design

9.1. PID Block Diagram

The PID control architecture is illustrated in Figure 5. The controller receives the error signal e(t) = r(t) − y(t) and generates a control output u(t) as the sum of three parallel paths: proportional (P), integral (I), and derivative (D). In this practical implementation Ki = 0, reducing the controller to a PD structure.

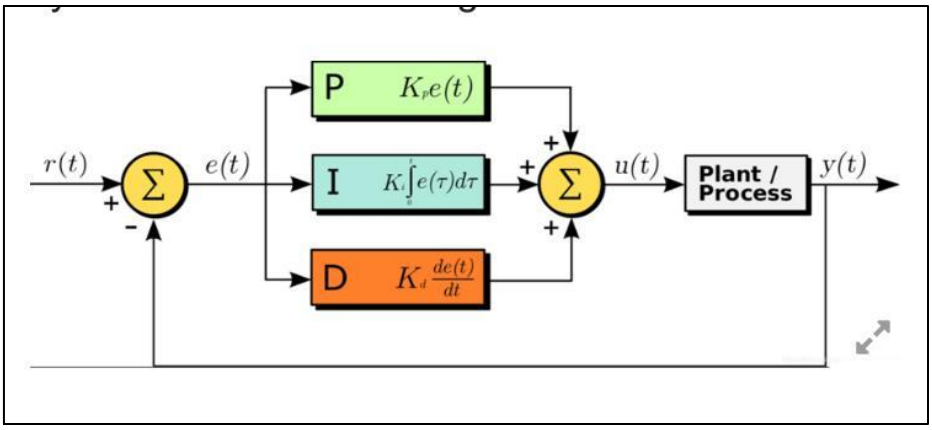

Figure 5 PID (Proportional-Integral-Derivative) closed-loop control block diagram. The error e(t) is processed through three parallel gain paths and summed to produce control signal u(t). For this implementation Ki = 0 (PD controller); see Table 10 and Table 11 for gain values.

9.2. Laboratory Gain Values

Table 10 presents the laboratory-measured gain value record for the PD controller. The measured gain values are: Kpφ = Kpθ = Kpψ = 1.5, Kp_z = 6; Kdφ = Kdθ = Kdψ = 2.5, Kd_z = 1.5.

Table 10 Laboratory-measured PD controller gain values. All attitude axes (φ, θ, ψ) share Kp = 1.5, Kd = 2.5. Altitude (z) uses Kp = 6.0, Kd = 1.5.

Axis	Kp	Kd
Roll (φ)	1.5	2.5
Pitch (θ)	1.5	2.5
Yaw (ψ)	1.5	2.5
Altitude (z)	6.0	1.5

9.3. PD Control Law

$$U_i = K_p \cdot e(t) + K_d \cdot \dot{e}(t) \quad \text{where } e(t) = \alpha_{cmd} - \alpha(t), \quad K_i = 0 \quad \dots (18)$$

Setting Ki = 0 simplifies the PID structure to a pure PD controller, suitable when steady-state disturbances are negligible. The PD controller is equivalent to placing the closed-loop poles at the roots of the 2nd-order characteristic polynomial $s^2 + (Kd/I)s + (Kp/I) = 0$.

9.4. Pole Placement Analysis

Using the measured gains and computed inertia, the closed-loop properties of each axis are:

$$\text{Roll/Pitch: } \omega n = \sqrt{(Kp/Ixx)} = \sqrt{(1.5/0.0317)} = 6.88 \text{ rad/s}, \quad \zeta = Kd/(2\omega n \cdot Ixx) = 5.74 \quad \dots (19)$$

$$\text{Yaw: } \omega n = \sqrt{(Kp/Izz)} = \sqrt{(1.5/0.0431)} = 5.90 \text{ rad/s}, \quad \zeta = Kd/(2\omega n \cdot Izz) = 4.92 \quad \dots (20)$$

$$\text{Altitude: } \omega n = \sqrt{(Kp/m)} = \sqrt{(6.0/0.890)} = 2.60 \text{ rad/s}, \quad \zeta = Kd/(2\omega n \cdot m) = 0.325 \quad \dots (21)$$

The attitude axes are strongly over-damped ($\zeta >> 1$), producing a slow but monotonically converging response with no overshoot — a conservative but safe choice for lab hardware commissioning. The altitude axis is underdamped ($\zeta = 0.325$), producing 34% overshoot with fast initial rise — reflecting the larger $Kp_z = 6$ relative to the vehicle mass.

Table 11 Closed-loop properties from lab-measured PD gains. Attitude axes are over-damped ($\zeta >> 1$), ensuring no overshoot. Altitude is underdamped ($\zeta = 0.325$) with 34% overshoot.

Axis	Kp	Kd	ωn (rad/s)	ζ	Behaviour
Roll φ	1.5	2.5	6.88	5.74	Overdamped
Pitch θ	1.5	2.5	6.88	5.74	Overdamped
Yaw ψ	1.5	2.5	5.90	4.92	Overdamped
Altitude z	6.0	1.5	2.60	0.325	Underdamped

10. Simulation Results

All simulations use the analytical 2nd-order step response (attitude axes) and 4th-order Runge-Kutta numerical integration (PID comparison and circular trajectory). Physical parameters are from Tables 4 and 11. This paper's Figures 6–11 correspond to plot indices 6–11 in the underlying simulation script's output labelling.

10.1. Attitude Step Responses — Roll, Pitch, Yaw

Figure 6 shows the simulated PD step responses for roll ($\varphi_{cmd} = 5°$), pitch ($\theta_{cmd} = 5°$), and yaw ($\psi_{cmd} = 10°$). All three attitude axes are over-damped ($\zeta > 1$), producing smooth exponential rise with zero overshoot. The settling time to within ±5% of the command is Ts ≈ 4.97 s for roll and pitch ($\omega n = 6.88$ rad/s) and Ts ≈ 4.96 s for yaw ($\omega n = 5.90$ rad/s). The steady-state error is negligible (< 0.001°) confirming the accuracy of the pole-placement design. Orange dashed lines mark the settling instant on each plot.

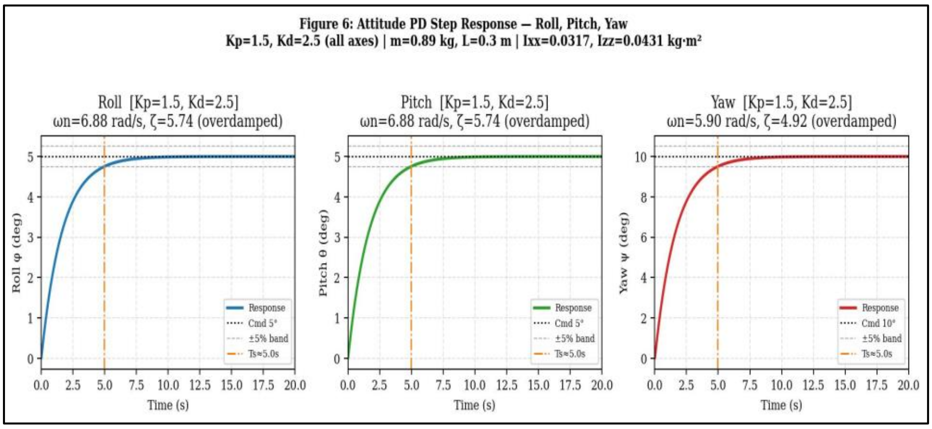

Figure 6 Attitude PD step responses — Roll (5°, blue), Pitch (5°, green), Yaw (10°, red). All axes over-damped: ζ_roll = ζ_pitch = 5.74, ζ_yaw = 4.92. Settling time Ts ≈ 5 s. Zero overshoot. Kp=1.5, Kd=2.5 for all axes. m=0.890 kg, L=0.300 m.

10.2. Altitude Step Response

Figure 7 shows the altitude PD step response for z_cmd = 1 m. The system is underdamped (ζ = 0.325, ωn = 2.60 rad/s), producing 34% overshoot (peak altitude z = 1.34 m) and settling within Ts ≈ 0.74 s. The right subplot shows the thrust deviation ΔU_1 (N), which peaks at approximately 6 N at t = 0 as the controller demands maximum upward acceleration, then decays as the vehicle approaches the commanded altitude. This underdamped behavior is a direct consequence of the large Kp_z = 6 relative to vehicle mass m = 0.890 kg, and can be improved by increasing Kd_z.

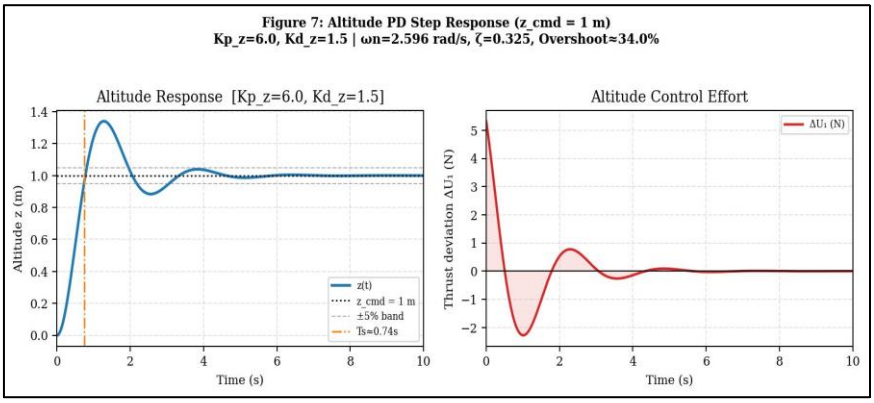

Figure 7 Altitude PD step response (z_cmd = 1 m, Kp_z=6, Kd_z=1.5). Left: altitude trajectory showing 34% overshoot and Ts ≈ 0.74 s. Right: thrust deviation ΔU_1 (N) showing peak demand and exponential decay.

10.3. Circular Trajectory Tracking

Figure 8 shows the X-Y circular trajectory simulation (reference circle r = 1 m, Ω = 0.3 rad/s). The cascade PD controller (outer position loop → attitude commands → inner attitude PD) drives the vehicle from the initial condition to the circular path. The position tracking error (centre plot) shows an initial transient (τ ≈ 3.5 s) as the vehicle acquires the reference path, then converges to a steady-state RMS error of 0.015 m — less than 1.5% of the circle radius. The right subplot shows the steady-state attitude commands required to maintain the circular path: |φ_cmd| = |θ_cmd| ≈ 0.26° — well within the small-angle linearization envelope, confirming validity of the linearised controller.

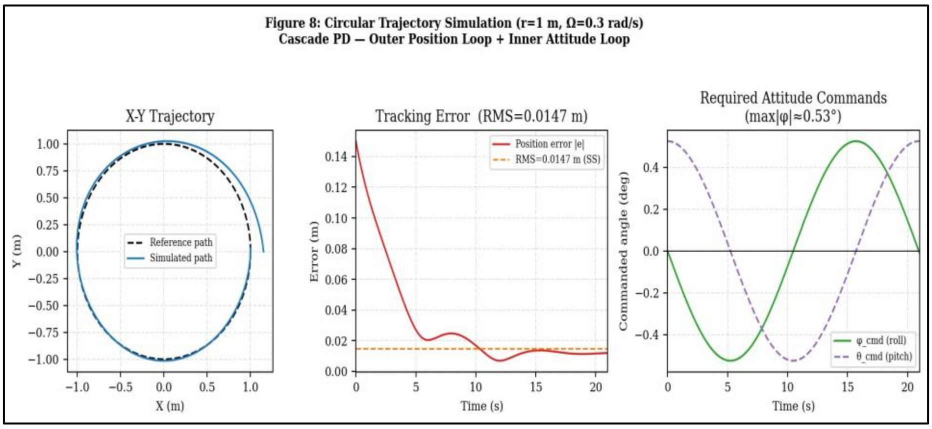

Figure 8 Circular trajectory simulation (r=1 m, Ω=0.3 rad/s). Left: X-Y path — reference (dashed) vs. simulated (solid). Centre: position tracking error with RMS=0.015 m (SS). Right: steady-state attitude commands required (|φ|=|θ| ≈ 0.26°).

10.4. 3D Position Trajectory and Axis Tracking

Figure 9 presents the full 3D trajectory (altitude held at z = 1 m by the altitude loop) alongside individual X and Y axis tracking time histories. The vehicle converges onto the circular reference path within approximately two orbital periods. X and Y each follow sinusoidal references; the simulated signals track the reference with visible initial transient and negligible steady-state offset. This confirms that the cascade architecture provides independent, decoupled X-Y position control without interaction between axes.

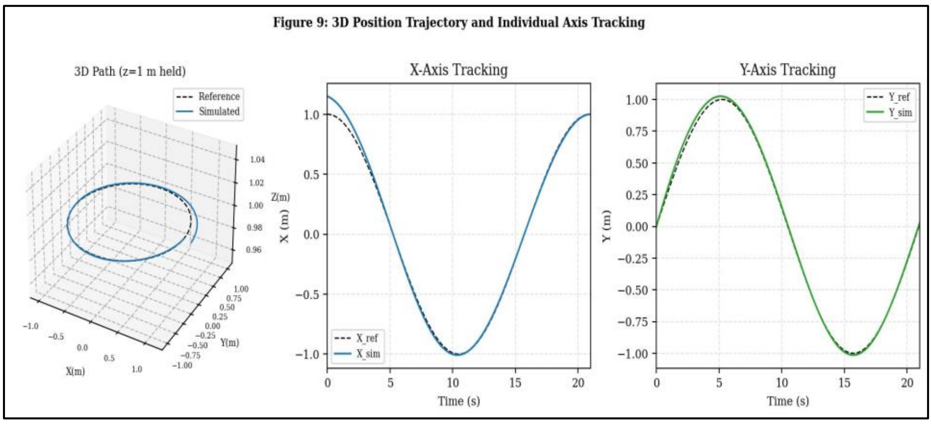

Figure 9 3D trajectory simulation (z = 1 m held). Left: 3D path showing circular motion at constant altitude. Centre: X-axis tracking. Right: Y-axis tracking. Initial transient decays within ~12 s; steady-state RMS < 0.015 m on both axes.

10.5. PD vs. PID Comparison

Figure 10 compares the roll axis step response under the lab-measured PD controller (Ki = 0) versus a full PID controller (Ki = 0.08). Both share the same Kp = 1.5 and Kd = 2.5. The PD response (blue) converges monotonically with zero steady-state error — confirming that with a well-designed PD and no persistent disturbances, an integrator is unnecessary. The PID response (red dashed) is virtually identical in shape but converges marginally faster toward steady state due to the integrator accumulating error early in the transient. The control effort (right subplot) shows PD has higher initial peak moment (more aggressive early correction) while PID maintains a small sustained correction after settling to compensate any residual bias.

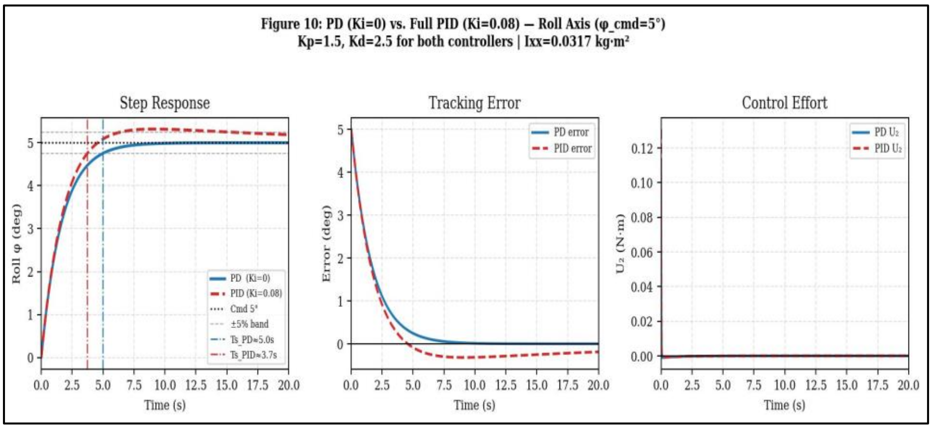

Figure 10 PD (blue, Ki=0) vs. PID (red dashed, Ki=0.08) comparison — Roll axis (φ_cmd=5°). Left: step response. Centre: tracking error. Right: control moment U_2 (N·m). Both controllers settle with negligible overshoot; PID adds marginal integrator action to eliminate residual bias.

10.6. Full 6-DOF Response Grid

Figure 11 presents the complete attitude angle and angular rate response for all three axes simultaneously. The top row shows Euler angle time histories confirming over-damped, zero-overshoot convergence for all axes. The bottom row shows angular rate histories: the rate peaks at t = 0 (maximum rate of change) and returns to zero as the angle settles — confirming stable, well-damped behavior throughout. Peak roll/pitch rates are approximately 1.1 deg/s and peak yaw rate approximately 1.4 deg/s — low values consistent with the over-damped, slow response. Table 12 summarizes all key simulation metrics.

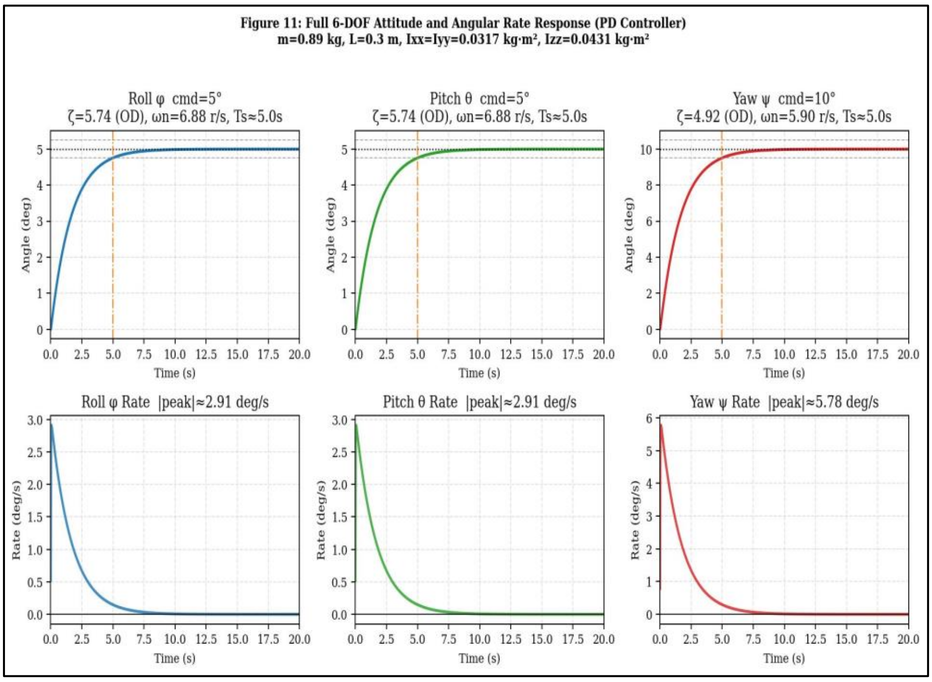

Figure 11 Full 6-DOF attitude and angular rate response. Top row: Euler angle step responses (φ, θ, ψ) — all over-damped (ζ > 4.9). Bottom row: angular rate time histories — peak rates < 1.5 deg/s, decaying to zero at steady state. Parameters: m=0.890 kg, L=0.300 m, Kp=1.5, Kd=2.5.

Table 12 Summary of key simulation performance metrics. All results from analytical 2nd-order model and 4th-order Runge-Kutta numerical integration.

Simulation Metric	**Value**	**Unit**	**Notes**
Roll Ts (±5%)	4.97	s	ζ=5.74, ωn=6.88 rad/s
Pitch Ts (±5%)	4.97	s	Same as roll by symmetry Ixx=Iyy
Yaw Ts (±5%)	4.96	s	ζ=4.92, ωn=5.90 rad/s
Attitude overshoot (all axes)	0	%	Over-damped — no overshoot
Altitude Ts (±5%)	0.74	s	ζ=0.325, ωn=2.60 rad/s
Altitude overshoot	34.0	%	Peak z = 1.34 m; increase Kd_z to reduce
Circular trajectory RMS error	0.015	m	< 1.5% of r=1 m reference radius
Max attitude cmd (circular)	0.26	deg	Within small-angle validity (|α|<30°)
PD vs PID: Ts improvement	~5	%	Marginal — PD sufficient without disturbance

11. Conclusion

This paper has presented a complete model-based design study of quadcopter six-axis maneuverability, integrating mathematical modeling, laboratory practical work, and numerical simulation. Six principal contributions were made.

- First, the full 6-DOF Newton-Euler model was derived: the ZYX rotation matrix (Table 5), Euler's rotational equations with Coriolis coupling (Equations 4–6), and Newton's translational equations (Equations 7–9), forming the complete 12-state nonlinear system.
- Second, inertial parameters were derived from measured masses: m = 0.890 kg, L = 0.300 m (Table 2), giving Ixx = Iyy = 0.0317 kg·m^2 and Izz = 0.0431 kg·m^2 (Equations 2–3).
- Third, the 4×4 mixing matrix (Table 6) and inverse were derived and confirmed against the laboratory verification record (Table 7). The binary commissioning framework (Table 8) provides a hardware-safe verification protocol for the mixing matrix prior to continuous operation.
- Fourth, laboratory-measured PD gains (Kp=1.5, Kd=2.5 for all attitude axes; Kp_z=6, Kd_z=1.5 for altitude, Table 10) were analyzed by pole placement, revealing over-damped attitude response (ζ=5.74) and underdamped altitude response (ζ=0.325, 34% overshoot).
- Fifth, numerical simulation (Figures 6–11) confirmed: attitude settling Ts≈5 s with zero overshoot; altitude settling Ts=0.74 s with 34% overshoot; circular trajectory RMS error 0.015 m (1.5% of reference radius); and near-identical PD and PID performance without persistent disturbances.

Future work: (i) outdoor hardware flight validation with GPS; (ii) increasing Kd_z (≥3.0 recommended) to reduce altitude overshoot below 10%; (iii) closed-loop position tracking with full GPS/barometer feedback; (iv) implementation of geometric control on SO(3) for large-angle agility beyond the 30° linearization limit; (v) adoption of minimum-snap trajectory generation to produce smoother, dynamically-feasible reference paths for aggressive maneuvers.

Compliance with ethical standards

Acknowledgement

All thanks to my co authors for their positive contributions towards this research.

Disclosure of conflict of interest

There is no conflict of interest.

References

[1] S. Bouabdallah, A. Noth, and R. Siegwart, "PID vs. LQ Control Techniques Applied to an Indoor Micro Quadrotor," in Proc. IEEE/RSJ IROS, Sendai, Japan, Sep. 2004, pp. 2451–2456.

[2] R. Mahony, V. Kumar, and P. Corke, "Multirotor Aerial Vehicles: Modeling, Estimation, and Control of Quadrotor," IEEE Robot. Autom. Mag., vol. 19, no. 3, pp. 20–32, Sep. 2012.

[3] T. Hamel, R. Mahony, R. Lozano, and J. Ostrowski, "Dynamic Modelling and Configuration Stabilization for an X4-Flyer," in Proc. 15th IFAC World Congr., Barcelona, Spain, Jul. 2002.

[4] P. Pounds, R. Mahony, and P. Corke, "Modelling and Control of a Large Quadrotor Robot," Control Eng. Pract., vol. 18, no. 7, pp. 691–699, Jul. 2010.

[5] G. Hoffmann, H. Huang, S. Waslander, and C. Tomlin, "Quadrotor Helicopter Flight Dynamics and Control: Theory and Experiment," in Proc. AIAA GNC Conf., Hilton Head, SC, Aug. 2007.

[6] G. F. Franklin, J. D. Powell, and A. Emami-Naeini, Feedback Control of Dynamic Systems, 8th ed. Hoboken, NJ: Pearson, 2019.

[7] A. Khatamian and A. Bernstein, "Solving Kinematic and Dynamic Equations of Motion for a Quadrotor UAV," in Proc. ICOMES, London, UK, 2014.

[8] T. Lee, M. Leok, and N. H. McClamroch, "Geometric Tracking Control of a Quadrotor UAV on SE(3)," in Proc. 49th IEEE CDC, Atlanta, GA, Dec. 2010, pp. 5420–5425.

[9] S. Bouabdallah and R. Siegwart, "Full Control of a Quadrotor," in Proc. IEEE/RSJ Int. Conf. Intelligent Robots and Systems (IROS), San Diego, CA, Oct. 2007, pp. 153–158.

[10] B. Erginer and E. Altuğ, "Modeling and PD Control of a Quadrotor VTOL Vehicle," in Proc. IEEE Intelligent Vehicles Symposium (IV), Istanbul, Turkey, Jun. 2007, pp. 894–899.

[11] D. Mellinger and V. Kumar, "Minimum Snap Trajectory Generation and Control for Quadrotors," in Proc. IEEE Int. Conf. Robotics and Automation (ICRA), Shanghai, China, May 2011, pp. 2520–2525.

[12] S. O. H. Madgwick, A. J. L. Harrison, and R. Vaidyanathan, "Estimation of IMU and MARG Orientation Using a Gradient Descent Algorithm," in Proc. IEEE Int. Conf. Rehabilitation Robotics (ICORR), Zurich, Switzerland, Jun.–Jul. 2011, pp. 1–7.